energies

MDPI

Article

Electric Vehicle Charging Station with Grid Support and Ancillary Service Capabilities

Moacyr Aureliano Gomes de Brito [1,*], Guilherme Mendonça dos Santos Martines [1], Matheus José de Sousa Coura [1], Ruben Barros Godoy [1] and Euzeli Cipriano dos Santos [2]

[1] Electrical Engineering Department, Faculty of Engineering, Architecture and Urbanism and Geography—FAENG, Federal University of Mato Grosso do Sul-UFMS, Costa e Silva Avenue, Campo Grande-MS 79070-900, Brazil; guilherme.martines@ufms.br (G.M.d.S.M.); matheus_sousa@ufms.br (M.J.d.S.C.); ruben.godoy@ufms.br (R.B.G.)

[2] Electrical and Computer Engineering, Purdue University, 799 W Michigan St. Indianapolis, West Lafayette, IN 46202, USA; edosssant@purdue.edu

* Correspondence: moacyr.brito@ufms.br

Abstract

This paper presents the power electronics architecture of an electric vehicle (EV) charging station operating as a DC microgrid with an AC grid interface. The grid-interface converter is implemented using an interleaved bidirectional DC–AC converter supporting bidirectional power exchange with the utility grid, as required for vehicle-to-grid (V2G) operation, while providing ancillary services to the utility grid. In addition to bidirectional power flow, the converter supports active power curtailment, reactive power compensation, and active power filtering, improving grid support and power quality. Within the DC microgrid, bidirectional converters manage the energy exchange between the DC bus, stationary battery storage, and electric vehicles. The EV charging stage is implemented using a set of parallel bidirectional dual active bridge (DAB) DC–DC converters, enabling galvanic isolation, high power density, and efficient bidirectional energy transfer between the DC bus and the vehicle batteries. To enhance the sustainability of the proposed system, a photovoltaic generation unit is connected to the DC bus through a dedicated interleaved power electronics converter. The control strategies and validation of the proposed architecture are presented with emphasis on converter operation and grid-support functionalities. The results demonstrate stable operation during battery charging and discharging, bidirectional power transfer between the EV battery and the DC bus through the DAB converter, bidirectional power exchange between the DC bus and the utility grid through the grid-interface converters, and a significant reduction in the total harmonic distortion (THD) of the grid currents while enabling advanced ancillary grid services.

Keywords: ancillary services; DC microgrid; electric vehicle charging station; grid support; power electronics converters

Academic Editors: Mustafa Tahir and Pierluigi Siano

Received: 24 September 2026
Revised: 4 November 2026
Accepted: 5 November 2026
Published: 7 November 2026

Copyright: © 2026 by the authors. Licensee MDPI, Basel, Switzerland. This article is an open access article distributed under the terms and conditions of the Creative Commons Attribution (CC BY) license.

1. Introduction

The rapid growth of electric vehicles (EVs) has intensified the need for efficient and flexible charging infrastructures capable of supporting both increasing energy demand and the operational requirements of modern power systems [1]. Conventional EV charging stations typically operate as passive loads connected to the distribution grid, which

may lead to power quality issues, demand peaks, and additional stress on grid assets, particularly when multiple stations operate concurrently [2]. To overcome these limitations, recent research has explored the adoption of advanced power electronics and control strategies, enabling charging stations to actively participate in grid operation. In this context, DC microgrid-based architectures have emerged as a promising solution due to their higher efficiency, reduced number of conversion stages, and improved capability to integrate distributed energy resources such as photovoltaic systems and energy storage units [3–5].

Furthermore, the integration of bidirectional power converters enables not only controlled EV charging but also vehicle-to-grid (V2G) functionalities, allowing EVs and stationary batteries to operate as distributed energy resources that can actively support grid operation [6–8].

In addition, advanced charging infrastructures can provide ancillary services such as active power regulation, reactive power compensation, and harmonic mitigation, contributing to improved grid stability and power quality [9]. The increasing penetration of renewable energy sources and distributed energy storage systems further reinforces the need for integrated solutions that combine energy management, bidirectional power flow, and efficient power conversion within a unified framework [10–13]. Complementary research has also addressed converter fault detection using signal-processing and convolutional neural network techniques [14], as well as optimization strategies for lithium-ion battery fast charging [15], which may contribute to the reliability and performance of future EV charging stations.

Despite these advancements, existing studies have primarily focused on specific aspects of EV charging stations, such as charging management, renewable energy integration, or bidirectional power flow. Although several studies address the combined operation of EV charging with renewable sources and energy storage systems, these functionalities are often treated at the control or energy management level rather than through a fully unified system architecture. In particular, limited attention has been given to charging station designs that simultaneously provide advanced grid-support functionalities while ensuring scalability through modular isolated converter structures. Furthermore, the integration of parallel isolated charging converters, renewable generation, stationary energy storage, and ancillary service provision within a single coordinated architecture remains a significant technical challenge.

Table 1 summarizes the main functional and architectural characteristics of representative studies, highlighting the differences between existing solutions and the proposed configuration.

Table 1. Comparison of functional and architectural features of related studies and the proposed EV charging station.

Feature	[3]	[4]	[6]	[13]	Proposed
PV Integration	Yes	Yes	Yes	Yes	Yes
Stationary battery storage	Yes	No	Yes	No	Yes
Bidirectional EV charging	* Yes	Yes	No	Yes	Yes
Interleaved grid-side converter	Yes	No	No	No	Yes
Parallel isolated DAB modules	No	No	No	No	Yes
Reactive power control	Yes	No	No	Yes	Yes
Shunt active power filtering	No	No	No	No	Yes
Four-leg grid converter	No	No	No	No	Yes
Validation approach	Experimental	Simulation	Simulation	Hil Simulation	Simulation

* Bidirectional charging for micromobility.

In this context, this paper proposes a DC microgrid-based EV charging station architecture that integrates renewable generation, stationary energy storage, and bidirectional EV charging within a unified system. The proposed solution employs a set of parallel dual active bridge (DAB) converters to enable modular and efficient EV charging, along with an interleaved bidirectional grid-interface converter that supports V2G operation and grid-support functionalities. An interleaved boost converter is adopted for photovoltaic integration, while an additional bidirectional converter interfaces stationary battery storage, enabling advanced energy management strategies that enhance renewable energy utilization and support power injection during peak demand periods. The effectiveness and performance of the proposed architecture are validated through the presented results.

The remainder of this paper is organized as follows. Section 2 presents the proposed system architecture and power converters. Section 3 describes the control strategies and grid-support functionalities while presenting the main outcomes. Section 4 discusses the results. Finally, Section 5 concludes the paper.

2. Materials and Methods

2.1. Proposed EV Charging Station Architecture

The proposed EV charging station is organized as a DC microgrid that integrates renewable energy generation, stationary energy storage, and bidirectional electric vehicle charging through a common DC bus. The architecture is designed to enable efficient energy management, modular scalability, and advanced grid-support functionalities. The system includes an interleaved bidirectional DC–AC converter that interfaces the DC microgrid with the utility grid, enabling bidirectional power flow and ancillary service capabilities. EV charging is performed through a set of parallel dual active bridge (DAB) converters, providing galvanic isolation, modularity, and bidirectional power transfer between the DC bus and vehicle batteries. In addition, a photovoltaic generation system is connected to the DC bus through an interleaved boost converter, while a stationary battery bank is interfaced via a bidirectional DC–DC converter, enabling energy storage, renewable energy utilization, and peak demand support.

2.1.1. System Overview

The proposed EV charging station is organized as a DC microgrid with a nominal DC bus voltage of 430 V, integrating renewable generation, stationary energy storage, bidirectional EV charging, and a grid-interface converter. The system is connected to a three-phase 220 V (line-to-line), 60 Hz utility grid through an interleaved bidirectional DC–AC converter rated at 22 kVA. The grid-interface stage is composed of two parallel-interleaved converters rated at 11 kVA each, enabling bidirectional power flow between the DC microgrid and the utility grid. In addition to the power exchange capability, one of the interleaved converters is implemented with a four-leg topology, allowing the system to operate as an active power filter providing harmonic mitigation and reactive power support.

Electric vehicle charging is performed through a modular structure composed of four parallel dual active bridge (DAB) converters, each rated at 5 kW, enabling scalable bidirectional power transfer between the DC bus and the EV batteries. The use of isolated DAB converters provides galvanic isolation, modularity, and flexibility for future system expansion. Renewable energy integration is achieved through a 7.4 kW photovoltaic system connected to the DC bus by means of an interleaved DC-DC boost converter. In addition, a stationary battery bank rated at 196 V and 100 Ah is interfaced to the DC bus through a 5 kW bidirectional DC–DC converter, enabling energy storage, renewable energy utilization during high solar irradiation periods, and power support during peak

demand or grid-support operation. The overall system architecture and power conversion stages are illustrated in Figure 1, while Table 2 summarizes the main power specifications of the EV charging station.

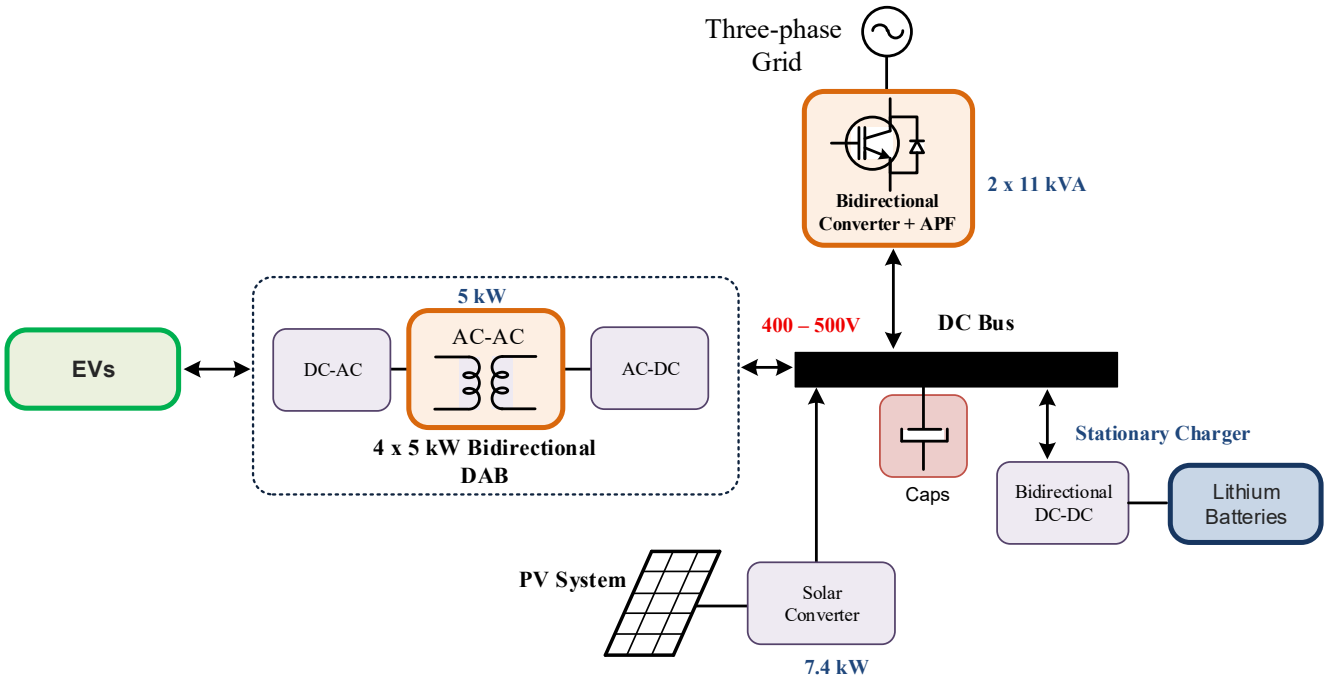


Figure 1. Overall system architecture.

Table 2. Main electrical parameters of the EV charging station.

Parameter	Value
DC bus voltage	430 V (400 V–500 V)
Grid voltage	3ϕ-220 V, 60 Hz
Grid Interface power	22 kVA
Active Filter capability	11 kVA
EV charger	4 × 5 kW
PV System	7.4 kW
Stationary battery	196 V, 100 Ah
DC-DC battery converter	5 kW

2.1.2. Grid Interface Converter

The grid-interface stage is responsible for regulating the DC bus voltage and managing the bidirectional power exchange between the DC microgrid and the utility grid. The converter is implemented as an interleaved bidirectional three-phase voltage-source inverter (VSI) with a total rated power of 22 kVA. The topology is composed of two parallel converters rated at 11 kVA each, operating with interleaved switching patterns in order to reduce current ripple, improve power density, and enhance overall system efficiency. Both converters employ sinusoidal pulse-width modulation (SPWM) at a switching frequency of 30 kHz, with a 180° phase shift between their triangular carriers. Figure 2 illustrates the proposed topology.

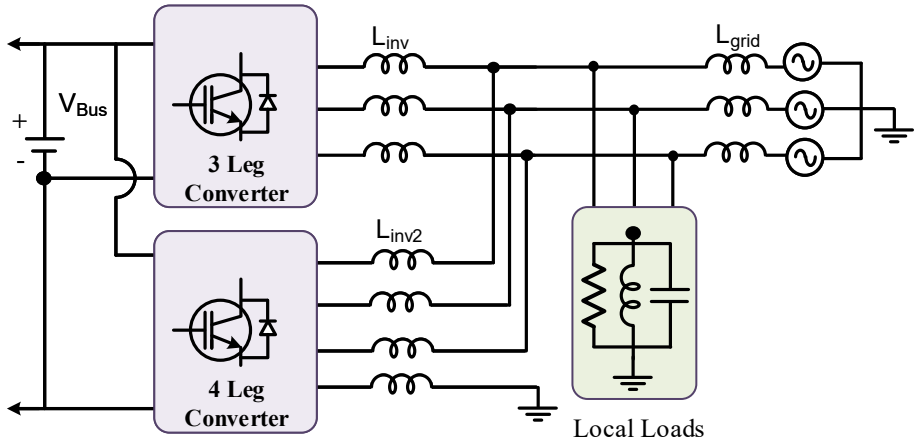


Figure 2. Proposed interleaved converter architecture.

The interleaving operation allows the sharing of power between the two converters while reducing the effective current ripple seen by the grid-side filter and the DC bus. This configuration also improves thermal distribution among the power semiconductor devices and increases the reliability of the system. Based on the aforementioned characteristics, the L-filter is adopted; hence, no damping strategy is necessary. More information about the selection of the output filter and damping strategies can be found in [16,17].

One of the interleaved converters is implemented with a four-leg topology, enabling the compensation of neutral current components and enhancing the capability of the system to operate as an active power filter. The interleaving strategy is applied to the three corresponding phase legs (a, b, and c) of both converters. The additional leg of the four-leg converter is independently controlled to provide neutral-current compensation and does not participate in the interleaving coordination between the converters. Therefore, the neutral-current compensation capability does not require any modification to the adopted 180° carrier phase shift. Through this configuration, the charging station can provide ancillary services to the grid, including harmonic current mitigation and reactive power compensation. The active filtering functionality is designed to provide up to 11 kVA of compensation capability, contributing to improved power quality at the point of common coupling.

The bidirectional operation of the grid-interface converter enables multiple operating modes, including grid-to-vehicle (G2V) power transfer, vehicle-to-grid (V2G) operation, renewable energy power injection, and support from the stationary battery system. In this way, the converter plays a central role in coordinating the power flow within the DC microgrid and enabling advanced grid-support functionalities.

2.1.3. EV Charging Converters

Electric vehicle charging is performed through a modular structure based on isolated dual active bridge (DAB) DC–DC converters [18,19]. The charging stage is composed of four parallel DAB modules, each rated at 5 kW, allowing a total EV charging capacity of up to 20 kW. This modular architecture enables scalable power capability, improved reliability, and flexible system expansion according to future charging requirements. Figure 3 illustrates the proposed configuration.

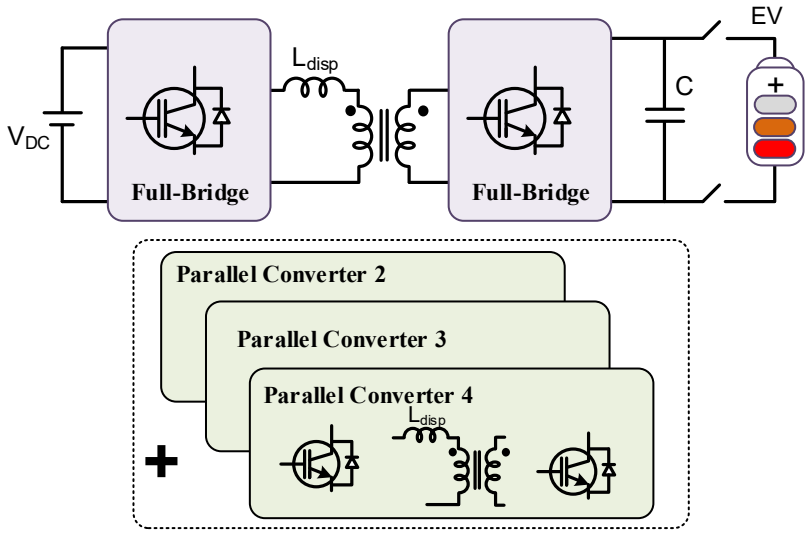


Figure 3. Parallel DAB EV charger.

Each DAB converter provides galvanic isolation between the DC microgrid and the EV battery through a high-frequency transformer. The primary side of the converter is connected to the 430 V DC bus, while the secondary side interfaces with the vehicle battery through an isolated DC link. The use of high-frequency isolation reduces transformer size and weight while ensuring electrical safety and compliance with EV charging standards [20].

The power transfer in the DAB converter is controlled through phase-shift modulation between the primary and secondary full bridges. By adjusting the phase shift between the switching signals, the converter regulates the power flow between the DC bus and the EV battery while maintaining bidirectional operation capability. This characteristic enables both conventional grid-to-vehicle (G2V) charging and vehicle-to-grid (V2G) operation when supported by the energy management system.

The parallel connection of multiple DAB modules enables current sharing among the converters and improves the overall efficiency of the charging stage. In addition, the modular configuration enhances fault tolerance, since individual modules can be disconnected or operated at reduced power without interrupting the operation of the entire charging station.

2.1.4. PV Interface Converter

The renewable energy source integrated into the proposed charging station is a photovoltaic (PV) generation system connected to the DC microgrid through an interleaved boost DC–DC converter. The PV system has a rated power of 7.4 kW and operates with an expected input voltage range between 220 V and 300 V, depending on the solar irradiance and temperature conditions of the photovoltaic array. The converter is responsible for stepping up this voltage to the nominal DC bus voltage of 430 V.

To improve efficiency and reduce current ripple, the PV interface employs a three-phase interleaved boost topology. The use of three interleaved cells allows the input current to be distributed among multiple switching stages, reducing current stress on the semiconductor devices and minimizing the ripple seen by the photovoltaic array. Additionally, the phase-shifted operation of the interleaved stages results in partial cancellation of the ripple components, enabling smaller passive components and improved dynamic performance. The topology is shown in Figure 4.

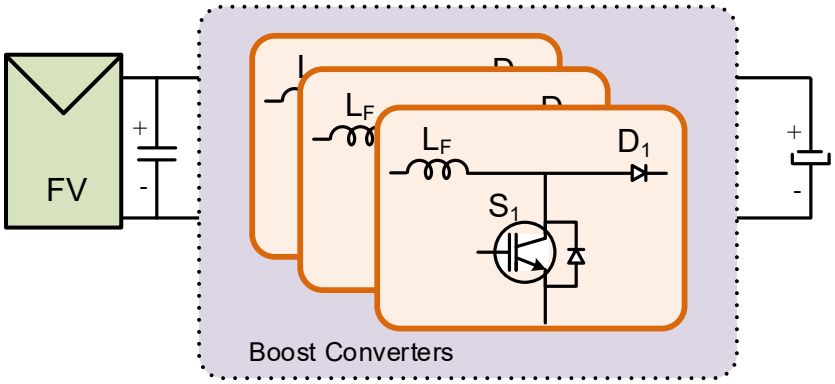


Figure 4. PV interface converter.

The converter operates under maximum power point tracking (MPPT) control to ensure maximum energy extraction from the PV array under varying environmental conditions. The harvested solar energy is primarily used to supply the EV charging converters and support the DC microgrid operation. When photovoltaic generation exceeds the local demand, surplus energy can be stored in the stationary battery bank or injected into the utility grid through the bidirectional grid-interface converter.

The integration of photovoltaic generation contributes to the sustainability of the charging station by reducing dependence on grid energy and enabling the direct utilization of locally generated renewable power within the DC microgrid.

2.1.5. Stationary Battery Interface Converter

The proposed EV charging station also incorporates a stationary battery energy storage system to enhance the operational flexibility of the DC microgrid and improve the utilization of renewable energy. The stationary battery bank has a nominal voltage of 196 V and a capacity of 100 Ah, and it is connected to the common DC bus through a 5 kW bidirectional DC–DC converter operating at a switching frequency of 40 kHz, as shown in Figure 5.

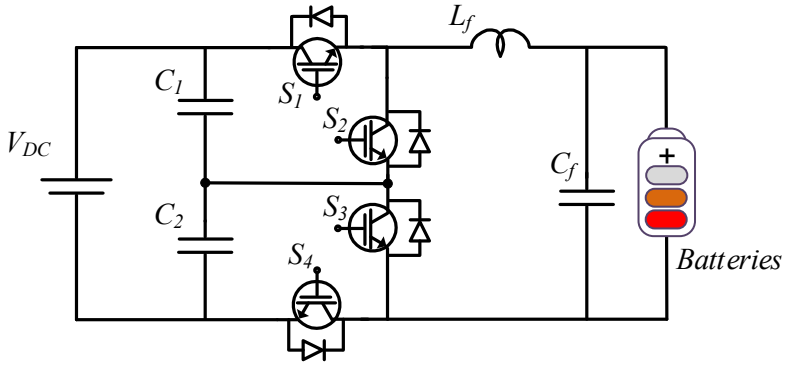


Figure 5. Three-level Buck/Boost DC-DC Stationary Battery Interface Converter.

The converter is responsible for regulating the power exchange between the battery bank and the DC microgrid, enabling both charging and discharging operation. During periods of high photovoltaic generation or low charging demand, the converter operates in battery charging mode, storing excess energy available in the DC bus. Conversely, during periods of high demand or when grid-support services are required, the converter operates in discharging mode, supplying energy from the battery bank to the DC bus.

This bidirectional capability allows the stationary storage system to perform multiple functions within the charging station. In addition to supporting EV charging, the battery

system enables energy shifting between high solar irradiation periods and peak demand intervals, contributing to improved energy management. Furthermore, the stored energy can be used to support grid-interactive functionalities, such as power injection during demand peaks or during the provision of ancillary services through the grid-interface converter.

The integration of stationary energy storage also contributes to stabilizing the DC bus voltage and improving the resilience of the charging station, allowing the system to maintain stable operation under varying generation and load conditions within the DC microgrid.

2.2. Control Strategy

The proposed EV charging station employs a hierarchical control structure designed to coordinate the operation of the different power converters connected to the DC microgrid. The control strategy aims to ensure stable DC bus voltage regulation, efficient energy exchange among the photovoltaic system, stationary battery storage, and EV charging converters, as well as controlled bidirectional power flow between the charging station and the utility grid.

At the system level, the DC bus voltage is used as the main coordination variable for the energy management of the microgrid. The grid-interface converter operates as the primary element responsible for regulating the DC bus voltage and managing the power exchange with the utility grid. Meanwhile, the photovoltaic converter operates under maximum power point tracking (MPPT) control to maximize renewable energy extraction, while the stationary battery converter manages energy storage and release according to the operating conditions of the DC microgrid.

The EV charging converters based on the dual active bridge (DAB) topology regulate the charging or discharging power of the connected vehicles through phase-shift control, enabling bidirectional energy transfer between the vehicle batteries and the DC bus. This configuration allows the system to support both conventional grid-to-vehicle (G2V) charging and vehicle-to-grid (V2G) operation.

In addition to power management within the DC microgrid, the grid-interface converter is also responsible for providing grid-support functionalities. These include active power regulation, reactive power compensation, and harmonic current mitigation through active filtering operation. The overall control structure enables coordinated operation of the different converters, ensuring stable system performance under varying load, renewable generation, and grid conditions.

The control strategies adopted for each power conversion stage are described in the following subsections.

2.2.1. DC Bus Voltage Control

The regulation of the DC bus voltage is essential for the stable operation of the proposed DC microgrid, since multiple power converters are connected to the common DC bus and operate under different power conditions. In the proposed architecture, the grid-interface converter is responsible for maintaining the DC bus voltage at its nominal value of 430 V.

The control structure employs a cascaded configuration composed of an outer DC bus voltage control loop and an inner current control loop implemented in the synchronous reference frame. The outer loop regulates the DC bus voltage by generating the reference for the active current component id^*. This current reference determines the amount of active power exchanged between the DC microgrid and the utility grid. A simplified diagram of this control scheme is depicted in Figure 6, where FTMFi represents the closed-loop current control.

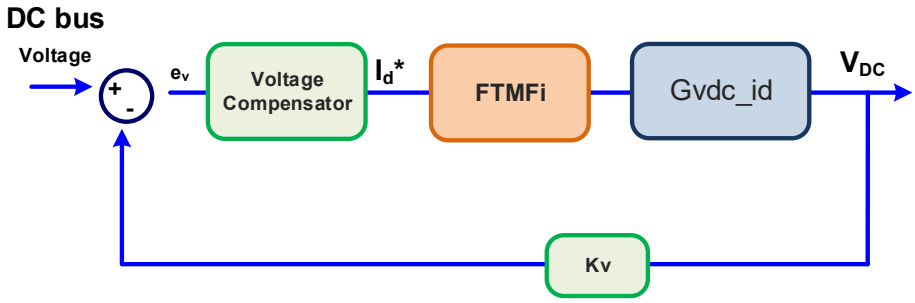


Figure 6. Control scheme for the DC bus regulation.

The voltage-to-current transfer function is obtained in the dq0 frame by means of the power balance between the DC bus and the power grid, as shown in (1). In (1), the power invariant formulation is used for the power grid calculation. In addition, by applying small-signal variations ($x = X + \Delta x$) and the Laplace Transform and noting that the derivative of a constant is zero and the grid voltage is imposed by the grid, one can find (3).

$$P_{DC} = P_{AC} => C\frac{dv_{DC}}{dt}v_{DC} = \frac{3}{2}v_d i_d \quad (1)$$

$$C\frac{d}{dt}(V_{DC} + \Delta v_{DC}) \times (V_{DC} + \Delta v_{DC}) = \frac{3}{2}V_d(I_d + \Delta i_d) \quad (2)$$

$$\frac{\Delta v_{DC}\,(s)}{\Delta i_D\,(s)} = \frac{3}{2}\frac{V_d}{V_{DC}}\frac{1}{sC} \quad (3)$$

where V_d is the peak grid phase-neutral voltage and V_{DC} is the nominal DC Bus voltage.

When the DC bus voltage increases due to excess power generation from the photovoltaic system or discharging of the stationary battery, the controller increases the active current reference to be injected into the grid. Conversely, when the DC bus voltage decreases due to increased EV charging demand, the converter absorbs power from the grid to restore the DC bus voltage. In this way, the grid-interface converter operates as the main element responsible for balancing the power flow within the DC microgrid.

The inner current controllers regulate the grid currents in the synchronous $dq0$ reference frame synchronized with the grid voltage using a phase-locked loop (PLL) [21,22]. This control structure ensures fast current regulation and stable operation of the grid-interface converter under varying load and generation conditions.

2.2.2. Reactive Power Control and Ancillary Services

Beyond the regulation of the DC bus voltage, the grid-interface converter is also responsible for providing grid-support and ancillary service functionalities. These services are implemented through the independent control of the current components in the synchronous $dq0$ reference frame.

Reactive power compensation is achieved through the control of the q-axis current component i_q. By adjusting the reference value i_q^*, the converter can inject or absorb reactive power from the grid, contributing to voltage support and improving the power factor at the point of common coupling. This functionality enables the charging station to operate as an active grid-support device while maintaining its primary charging functions.

In addition to reactive power control, the system is capable of performing harmonic current compensation using an active filtering strategy based on the synchronous reference frame (SRF) method [23,24]. In this approach, the grid currents are transformed to

the synchronous dq0 frame, where the oscillating components associated with harmonic distortion appear as alternating signals. By extracting and compensating the oscillating current components, the converter generates reference currents that cancel the harmonic components present in the grid currents.

The four-leg topology implemented in one of the interleaved grid converters enables the control of the zero-sequence current component i_0, allowing the system to compensate neutral currents and improve the performance of the active filtering operation. Consequently, the overall control strategy based on the d, q, and i_0 current references enables the simultaneous provision of active power regulation, reactive power compensation, and harmonic mitigation, allowing the EV charging station to provide ancillary services while maintaining stable DC microgrid operation. The control strategy of the grid-interface converters is depicted in Figures 7 and 8.

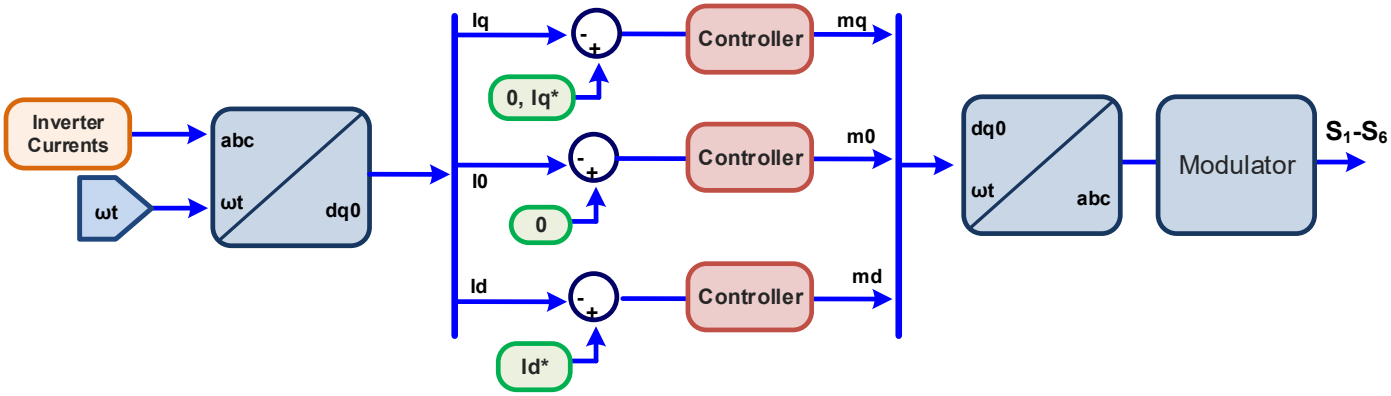


Figure 7. Control scheme for the interleaved inverter for active power injection and reactive power compensation.

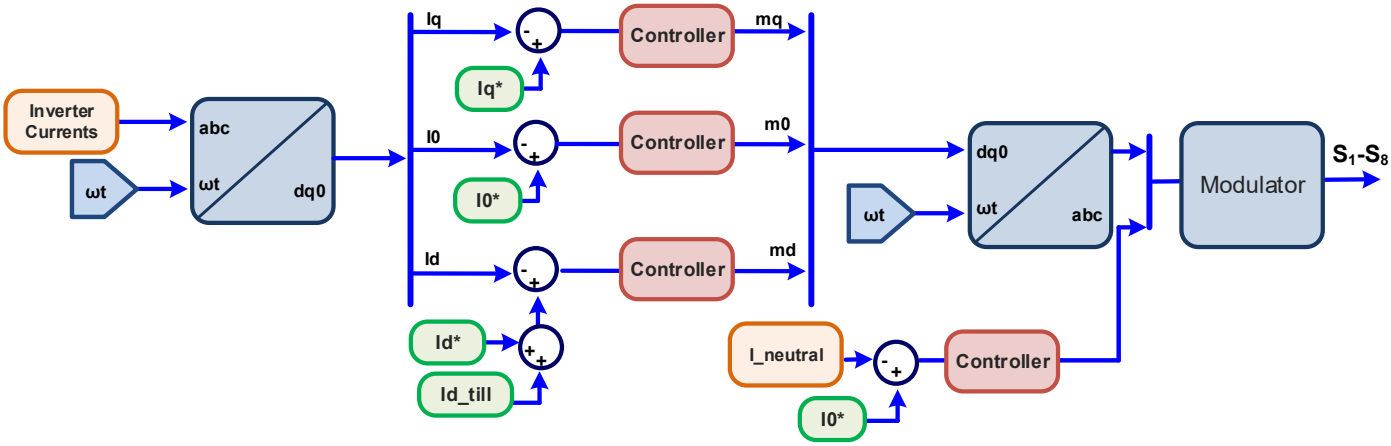


Figure 8. Control scheme for the second interleaved inverter with ancillary services.

The analysis and extraction of the load components are done using the auxiliary scheme of Figure 9.

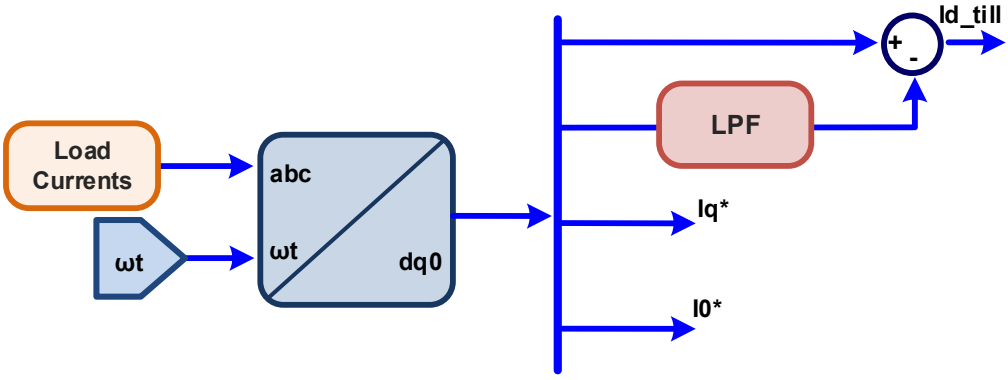


Figure 9. Strategy for extraction of the load components.

The current-to-modulation index transfer functions are obtained in the dq0 frame by using the single-phase equivalent model [23]. Each phase of the active filter is connected to the grid using a first-order filter (L_f and R_f). The voltage produced by the inverter at each inverter leg is dependent on the product of the modulation index m by the DC bus voltage— V_{BUS}. Thus, (4) can be written using Kirchhoff's voltage law.

$$m_x V_{BUS} = v_x + R_f i_x + L_f \frac{di_x}{dt} + R_f i_n + L_f \frac{di_n}{dt} \tag{4}$$

where $x = a, b, c$. R_f and L_f represent the resistance and inductance of the filter inductors.

Substituting x for all phases, summing up the equations and observing that $i_a + i_b + i_c = i_n$ it is possible to find (5)–(7), in function of the current's derivatives:

$$L_f \frac{di_a}{dt} = -R_f i_a + \frac{V_{BUS}}{4}(3m_a - m_b - m_c) + \frac{1}{4}(-3v_a + v_b + v_c) \tag{5}$$

$$L_f \frac{di_b}{dt} = -R_f i_b + \frac{V_{BUS}}{4}(-m_a + 3m_b - m_c) + \frac{1}{4}(v_a - 3v_b + v_c) \tag{6}$$

$$L_f \frac{di_c}{dt} = -R_f i_c + \frac{V_{BUS}}{4}(-m_a - m_b + 3m_c) + \frac{1}{4}(v_a + v_b - 3v_c) \tag{7}$$

In matrix form, one can rewrite (5)–(7) as (8):

$$L_f \frac{d}{dt}\left(\begin{bmatrix} i_a \\ i_b \\ i_c \end{bmatrix}\right) = R_f \begin{bmatrix} -1 & 0 & 0 \\ 0 & -1 & 0 \\ 0 & 0 & -1 \end{bmatrix} \begin{bmatrix} i_a \\ i_b \\ i_c \end{bmatrix} + \frac{V_{BUS}}{4} \begin{bmatrix} 3 & -1 & -1 \\ -1 & 3 & -1 \\ -1 & -1 & 3 \end{bmatrix} \begin{bmatrix} m_a \\ m_b \\ m_c \end{bmatrix} + \frac{1}{4} \begin{bmatrix} -3 & 1 & 1 \\ 1 & -3 & 1 \\ 1 & 1 & -3 \end{bmatrix} \begin{bmatrix} v_a \\ v_b \\ v_c \end{bmatrix} \tag{8}$$

Using the direct abc to dq0 transform [25], called T, and its inverse (T^{-1}), and using some mathematical manipulations, one can reach (10).

$$\begin{aligned} T \times L_f \frac{d}{dt}\left(T^{-1}\begin{bmatrix} i_a \\ i_b \\ i_c \end{bmatrix}\right) &= T \times \left(R_f \begin{bmatrix} -1 & 0 & 0 \\ 0 & -1 & 0 \\ 0 & 0 & -1 \end{bmatrix} T^{-1} \begin{bmatrix} i_d \\ i_q \\ i_0 \end{bmatrix}\right) + T \times \left(\frac{V_{BUS}}{4} \begin{bmatrix} 3 & -1 & -1 \\ -1 & 3 & -1 \\ -1 & -1 & 3 \end{bmatrix} T^{-1} \begin{bmatrix} m_d \\ m_q \\ m_0 \end{bmatrix}\right) \\ &+ T \times \left(\frac{1}{4} \begin{bmatrix} -3 & 1 & 1 \\ 1 & -3 & 1 \\ 1 & 1 & -3 \end{bmatrix} T^{-1} \begin{bmatrix} v_d \\ v_q \\ v_0 \end{bmatrix}\right) \end{aligned} \tag{9}$$

$$\frac{d}{dt}\begin{bmatrix} i_d \\ i_q \\ i_0 \end{bmatrix} = \begin{bmatrix} -\frac{R_f}{L_f} & \omega & 0 \\ -\omega & -\frac{R_f}{L_f} & 0 \\ 0 & 0 & -\frac{R_f}{L_f} \end{bmatrix}\begin{bmatrix} i_d \\ i_q \\ i_0 \end{bmatrix} + \frac{V_{BUS}}{4L_f}\begin{bmatrix} 4 & 0 & 0 \\ 0 & 4 & 0 \\ 0 & 0 & 1 \end{bmatrix}\begin{bmatrix} m_d \\ m_q \\ m_0 \end{bmatrix} + \frac{1}{4L_f}\begin{bmatrix} -4 & 0 & 0 \\ 1 & -4 & 0 \\ 0 & 0 & -1 \end{bmatrix}\begin{bmatrix} v_d \\ v_q \\ v_0 \end{bmatrix} \quad (10)$$

The grid voltages at (10) are disturbances for the system. By applying the Laplace Transform to each sequence of equations and adding the decoupling terms, it is possible to obtain the current-to-modulation-index transfer functions as in (11) and (12).

$$G_{id,iq}(s) = \frac{V_{BUS}}{sL_{inv} + R_{Linv}} \quad (11)$$

$$G_{i0}(s) = \frac{1}{4}\left(\frac{V_{BUS}}{sL_{inv} + R_{Linv}}\right) \quad (12)$$

where V_{BUS} is the DC Bus voltage, L_f is the inductance and R_f is the resistance of the output filter. For the d and q axes, the transfer function is shown as (11), whereas for the 0 axis it is shown as (12). As one can observe, the neutral current experiences an impedance four times higher once its current is provided by all phases.

The controllers of the DC bus voltage and grid current control loops were designed using a frequency-domain approach based on Bode analysis. The controller gains were determined considering the crossover frequency and phase margin, with the inner current loop designed to operate faster than the outer DC bus voltage loop, ensuring an appropriate separation between their dynamics.

2.2.3. EV Charging Interface Converter Control

Electric vehicle charging is performed through a modular structure composed of four parallel dual active bridge (DAB) converters, each rated at 5 kW. The use of isolated DAB converters provides galvanic isolation between the EV batteries and the DC microgrid while enabling bidirectional power transfer required for both grid-to-vehicle (G2V) and vehicle-to-grid (V2G) operation. In addition, the modular architecture allows scalability of the charging station by adding or removing converter modules according to the required charging capacity, as previously mentioned.

Each DAB converter operates based on phase-shift modulation between the primary and secondary full-bridges. By controlling the phase-shift angle ϕ between the square-wave voltages applied to the high-frequency transformer, the amount and direction of the transferred power can be regulated. Under this operating principle, the transferred power can be approximated by (13) [26].

$$P = \frac{\eta V_1 V_2}{\omega L}\phi\left(1 - \frac{\phi}{\pi}\right), \quad (13)$$

where V_1 (equal to V_{BUS} and V_2) are the DC voltages on the primary and secondary sides of the converter, n is the transformer turns ratio, L is the equivalent leakage inductance referred to the primary side, ω is the switching angular frequency, and ϕ represents the phase shift between the bridge voltages.

The charging control is implemented through a power regulation loop that generates the reference phase shift for each DAB module. This structure allows the regulation of the charging current delivered to the EV battery while maintaining stable interaction with the DC bus. During V2G operation, the same control structure enables the controlled transfer of energy from the vehicle battery back to the DC microgrid. To smooth the battery

current, a series inductance is inserted after the output capacitor of the second DAB. The battery is modeled as a DC voltage source with its series resistance (V_{bat}; R_{bat}).

Starting from (13), the power P can be varied as a function of ϕ and V_2. Thus, (14) is found in terms of the derivatives of such quantities as

$$\Delta P = \frac{dP}{d\emptyset}\Delta\emptyset + \frac{dP}{dV_2}\Delta V_2 = K_\emptyset \Delta\emptyset + K_{V_2}\Delta V_2 \quad (14)$$

where $\frac{dP}{d\emptyset} = \frac{\eta V_1 V_2}{\omega L}\left(1 - \frac{2\phi}{\pi}\right)$ and $\frac{dP}{dV_2} = \frac{\eta V_1}{\omega L}\phi\left(1 - \frac{\phi}{\pi}\right)$.

The dynamics of the capacitor power (P_C) in function of the DAB power and the battery power (Po) is shown as (15) and (16):

$$P_C = P - P_0 \quad (15)$$

$$C\frac{dv_C}{dt}v_c = P - P_0 \quad (16)$$

The dynamics of the inductor in terms of the battery power are shown as (17) and (18):

$$L\frac{di_o}{dt} = v_c - V_{bat} - R_{bat}i_o \quad (17)$$

$$L\frac{dP_o/V_{bat}}{dt} = v_c - V_{bat} - R_{bat}\frac{P_o}{V_{bat}} \quad (18)$$

Linearizing (18) and (16), and considering V_{bat} constant, one can obtain (19) and (20).

$$C\frac{d\Delta v_C}{dt}V_c = \Delta P - \Delta P_0 = K_\emptyset\Delta\emptyset + K_{V_2}\Delta V_2 - \Delta P_0 \quad (19)$$

$$\frac{L}{V_{bat}}\frac{d\Delta P_o}{dt} = \Delta v_c - \frac{R_{bat}}{V_{bat}}\Delta P_o \quad (20)$$

Applying the Laplace Transform in (19) and (20) and verifying that V_2 equals Vc, one can reach (21) that drives the dynamics of the power regulation loop as a function of the phase angle.

$$\frac{\Delta P_o\,(s)}{\Delta\emptyset\,(s)} = \frac{K_\emptyset V_{bat}}{\left[s^2 LCV_C + \left(R_{bat}CV_C - K_{V_2}L\right)s + \left(V_{bat} - K_{V_2}R_{bat}\right)\right]} \quad (21)$$

Since multiple DAB converters operate in parallel, a power-sharing strategy is adopted to ensure balanced operation among the modules. Each converter receives a common power reference derived from the charging management system, and the reference is equally distributed among the four modules. This approach ensures uniform current sharing and prevents overloading of individual converters, improving the reliability and efficiency of the charging system.

The modular DAB architecture combined with phase-shift control enables flexible and efficient EV charging while maintaining bidirectional power capability and compatibility with the DC microgrid energy management strategy.

2.2.4. PV MPPT Control Strategy

The main objective of this control system is to extract the maximum available power from the photovoltaic array under varying environmental conditions. For this purpose, a maximum power point tracking (MPPT) algorithm generates the reference value for the photovoltaic voltage $V_{PV}*$, corresponding to the optimal operating point of the PV array.

The converter control regulates the PV voltage by adjusting the duty cycle of the interleaved boost stages. A review of MPPT algorithms can be found in [27].

In the proposed system, the photovoltaic current is not directly measured. Instead, it is estimated based on the photovoltaic power, the measured PV voltage, and the instantaneous duty cycle of the boost converter. This estimation approach enables the determination of the PV current and generated power without requiring a dedicated current sensor, reducing system complexity and cost while still providing the necessary information for monitoring and energy management functions.

The interleaved structure distributes the power among the three boost phases and significantly reduces the input current ripple at the PV terminals. The harvested photovoltaic energy is injected into the DC bus, where it can be directly used to supply the EV charging converters, charge the stationary battery system, or be exported to the utility grid through the grid-interface converter.

The flowchart of the implemented algorithm is depicted in Figure 10. Details on how to implement the MPPT algorithm and tune a controller for such a purpose can be found in [28–30]. Finally, the estimation of the boost current is based on [31].

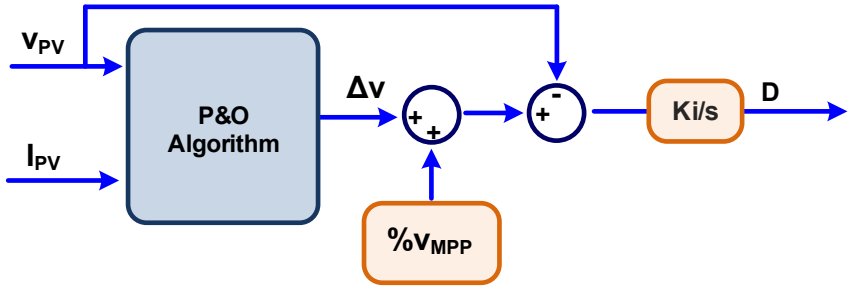


Figure 10. Mixed MPPT Control Strategy.

2.2.5. Stationary Battery Energy Management

The stationary battery energy storage system is integrated into the DC microgrid to increase the operational flexibility of the charging station and improve the utilization of renewable energy resources. The battery bank is interfaced to the DC bus through a bidirectional DC–DC converter that enables controlled charging and discharging operation.

The control strategy is based on regulating the battery current according to the operating conditions of the DC microgrid. During periods of high photovoltaic generation and low charging demand, the converter operates in charging mode, storing the excess energy available on the DC bus. Conversely, during periods of high demand or when grid-support operation is required, the converter operates in discharging mode, injecting power from the battery bank into the DC microgrid.

This energy management approach allows the system to perform energy shifting between periods of high solar generation and peak demand intervals. As a result, the stationary battery system contributes to reducing the dependence on the utility grid and improving the overall efficiency of the charging station.

In addition, the battery storage system supports the operation of the grid-interface converter by helping stabilize the DC bus voltage during rapid variations in load or renewable generation. This capability enhances the dynamic performance of the DC microgrid and improves the reliability of the EV charging infrastructure.

3. Results

This section presents simulation results to validate the operation and performance of the proposed EV charging station architecture. The results are organized into different operational scenarios in order to evaluate the main functionalities of the system, including

DC bus regulation, EV charging operation, renewable energy integration, stationary battery management, grid-support capabilities, active power filtering, and multifunctional performance. Table 3 summarizes the elements of each power electronics converter, whereas Table 4 presents the controllers used in each control loop. The simulations were performed in MATLAB/Simulink R2021a using the ode23tb variable-step solver, with a maximum step size of 1×10^{-6} s and a relative tolerance of 1×10^{-3}. The converter models include the default on-state resistances of the MOSFETs and additional series resistances associated with the passive components, as specified in Table 3. These resistances improve Simulink numerical behavior. Since the study focuses on system-level operation and control performance, a detailed semiconductor loss analysis is beyond its scope. The switching frequencies were set to 50 kHz for the DAB converters, 30 kHz for the grid-interface inverters and the three-phase interleaved boost converter, and 40 kHz for the three-level bidirectional buck–boost DC–DC converter.

Table 3. Main elements of the power electronics converters.

Element	Acronym	Value
Grid output filter inductance	L_{inv}	560 µH
Grid output filter series resistance	R_{inv}	0.05 Ω
DC Bus capacitance	C_{bus}	6 mF
DAB leakage inductance	L_{disp}	22 µH
DAB leakage series resistance	R_{dab}	0.02 Ω
DAB output filter capacitance	C_{bat}	47 µF
DAB output capacitor ESR	RC_{bat}	0.01 Ω
DAB output filter inductance	L_{bat}	400 µH
Boost input filter capacitance	C_{PV}	10 µF
Boost inductance	L_b	520 µH
Boost output filter capacitance	C_b	15 µF
Three-level DC-DC bus capacitance	C_1 and C_2	22 µF
Three-level DC output filter capacitance	C_f	2.2 µF
Three-level DC output filter inductance	L_f	150 µH

Table 4. Controller parameters.

System	Strategy	Controller (Gains)
DC bus voltage control	Integral plus proportional controller	$K_p = 0.35$ and $K_i = 14.15$
dq0 grid current control	Integral plus proportional controller	$K_p = 0.028$ and $K_i = 208.18$
MPPT extraction for the interleaved DC-DC converter	P&O algorithm plus Vcte Controlled by an integral action	$V_{cte} = 270V$; ΔV = 0.5V and $K_i = -0.3$
Phase-shift control for the DAB converters	Zero-pole compensation	$0.0005 \times \frac{(s+729.3)^2}{s(s+314160)}$
Three-level DC-DC battery controller	Integral plus proportional controller	$K_p = 0.01$ and $K_i = 1$

3.1. DC Bus Regulation

This scenario evaluates the regulation capability of the DC microgrid bus under dynamic operating conditions. The objective is to verify the effectiveness of the grid-interface converter in maintaining the DC bus voltage at its nominal value while exchanging active power with the utility grid. Transient events are applied to assess the stability and dynamic response of the DC bus control, as can be seen in Figure 11. One can verify the performance of the DC bus regulation control, which maintains the stability of the voltage at the DC bus. For a 33% power step, the voltage undershoot and overshoot are less than 10%, with the voltage returning to its nominal value within 0.05 s. For the cascaded DC bus voltage and grid current control structure, the frequency-domain analysis indicates crossover frequencies of approximately 7.63 Hz and 3.60 kHz for the outer voltage and inner current loops, respectively. The corresponding phase margins are approximately 49.8° and 72.0°, based on continuous-time models without considering digital implementation and PWM delays. The significant separation between the crossover frequencies supports the coordinated operation of the two control loops.

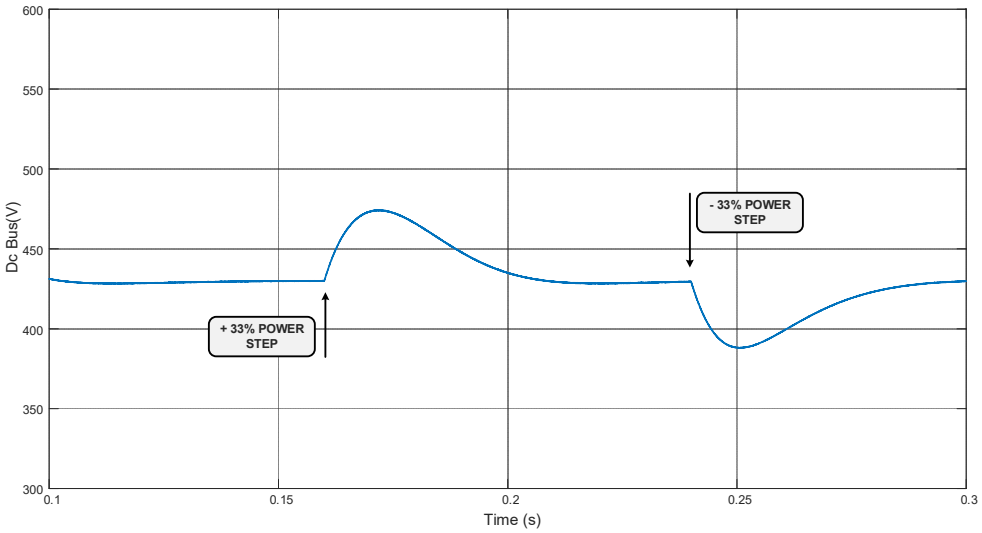


Figure 11. DC bus voltage during transients of power (more and minus 33%).

3.2. EV Charging Operation

This scenario analyzes the operation of the EV charging stage based on the parallel DAB converters. The objective is to evaluate the modular charging capability and the prescribed equal power sharing among the converters when supplying energy to electric vehicles. Different charging power levels are considered in order to demonstrate the scalability and flexibility of the proposed charging architecture. Figure 12 presents the SoC rising from 80%, while Figure 13 shows the aggregate charging power profile as the DAB converters are sequentially initiated and smoothly start charging the battery pack. Each DAB converter is equipped with an independent power controller, allowing its phase-shift angle to be adjusted individually to track the assigned power reference. Since all modules supply the same EV battery, they operate with a common secondary-side voltage. Equal power sharing was arranged through identical power references for the DAB modules under nominal operating conditions, while the effects of parameter mismatch, module unavailability, and wide battery voltage variations were not evaluated in this study.

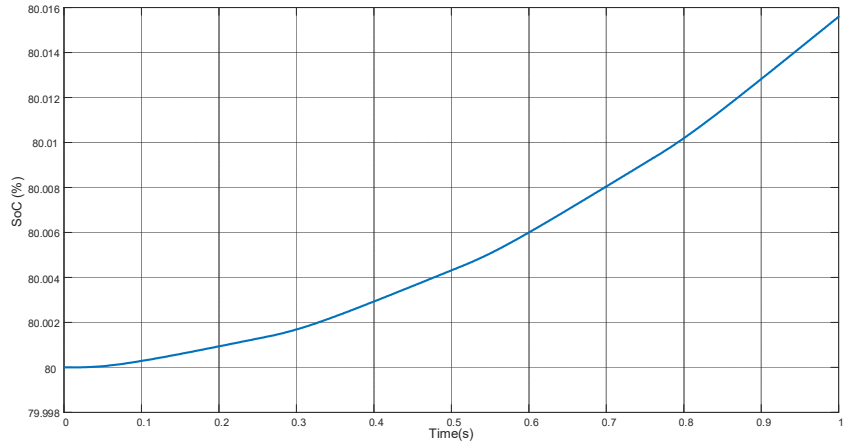


Figure 12. SoC increase due to charging.

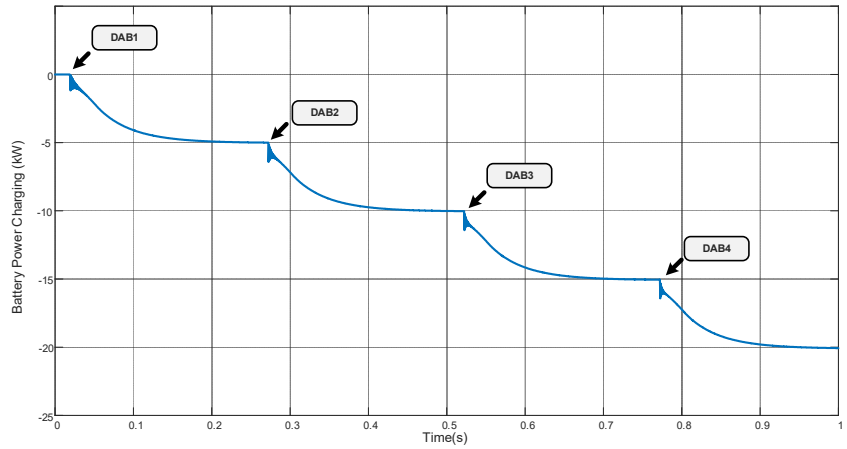


Figure 13. Battery charging power and the instant of initialization of each DAB converter.

Figure 14 illustrates the bidirectional operation of one DAB converter under different operating conditions. Figure 14a presents the transition between battery charging (G2V), zero-power operation, and battery discharging (V2G). The waveforms correspond to the first full-bridge voltage (blue), the second full-bridge voltage (red), and the leakage inductance current (yellow), with the current multiplied by 10 for visualization purposes. Figure 14b–d show detailed waveforms for each operating mode. The reversal of the phase shift between the full-bridge voltages demonstrates the change in the direction of power transfer, while the zero-power condition is characterized by approximately synchronized bridge voltages and negligible leakage inductance current. The EV battery was represented using the generic lithium-ion battery model available in MATLAB/Simulink, with a nominal voltage of 400 V, a rated capacity of 50 Ah, an initial state of charge of 80%, and a response time of 30 s. The remaining battery parameters were determined from the nominal characteristics using the model's default parameterization, as summarized in Table 5. Temperature and aging effects were not considered.

The variations in the amplitude of the first full-bridge voltage (blue waveform) in Figure 14a reflect the DC-bus voltage response to changes in power flow, as the grid-interface converters adjust their power exchange with the utility grid to maintain DC-bus voltage regulation.

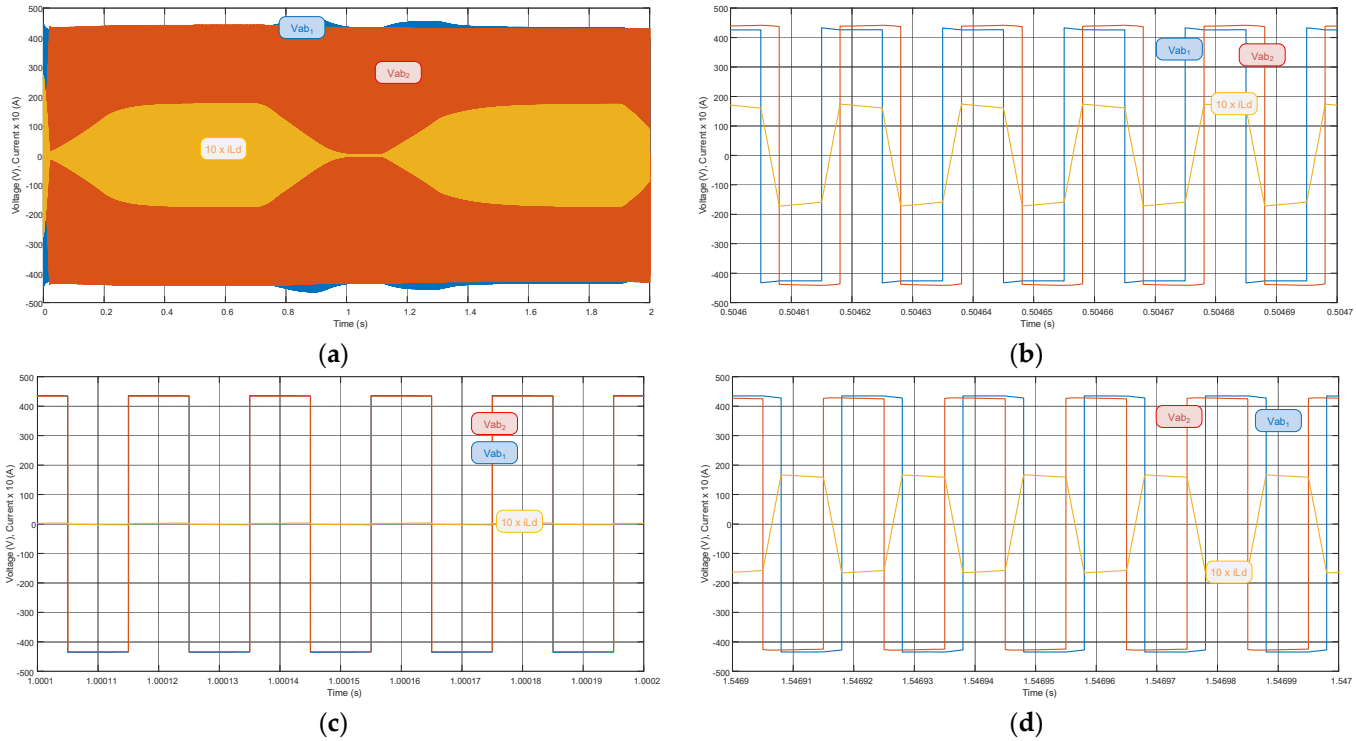


Figure 14. Voltage waveforms of the first and second full-bridge stages and leakage inductance current of one DAB converter: (**a**) transitions between G2V, zero-power, and V2G operation; (**b**) detailed waveforms during G2V operation; (**c**) detailed waveforms under zero-power conditions; and (**d**) detailed waveforms during V2G operation.

Table 5. Parameters of the EV lithium-ion battery model.

Parameter	Value
Battery model	Lithium-ion (MATLAB/Simulink)
Nominal voltage	400 V
Rated capacity	50 Ah
Initial state of charge (SoC)	80%
Internal resistance	0.08 Ω
Fully charged voltage	465.59 V
Cut-off voltage	300 V
Battery response time	30 s

3.3. Photovoltaic Integration

This scenario evaluates the integration of the photovoltaic generation system into the DC microgrid. The performance of the interleaved boost converter and the MPPT control strategy is analyzed under varying solar generation conditions. The objective is to verify the capability of the system to extract maximum power from the PV array and transfer it to the DC bus. Figure 15 presents the currents through each boost inductance to show the interleaving property. Figure 16 shows the PV curves for two distinct operating points. The blue curve represents the PV generation at 1000 W/m² and 25 °C; the red curve shows the PV power at 800 W/m² and 45 °C. The PV array consists of 14 modules arranged in 2 parallel branches. Each PV module has a rated power of approximately 530 Wp with a V_{MPP} of 40 V. The MPPT efficiency exceeds 99%, indicating that the PV array operates close to its maximum power point, with negligible power ripple, as shown in Figure 17.

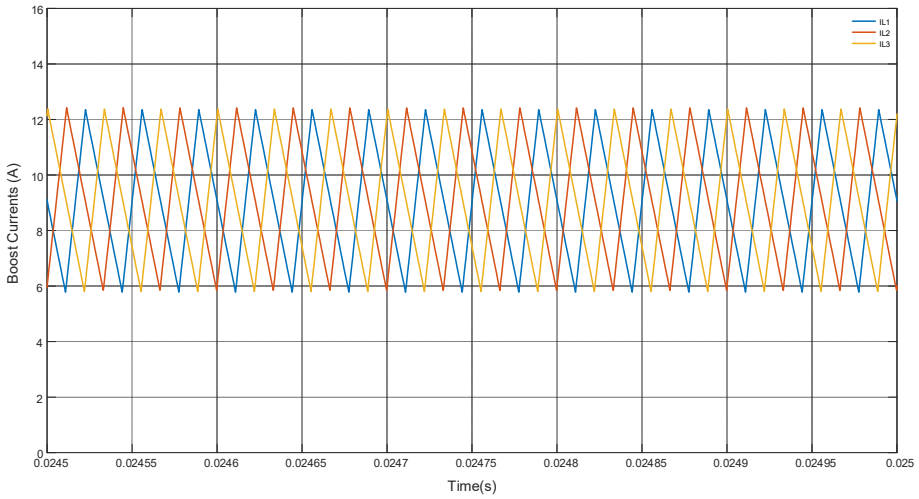


Figure 15. Current through the 3 boost inductances.

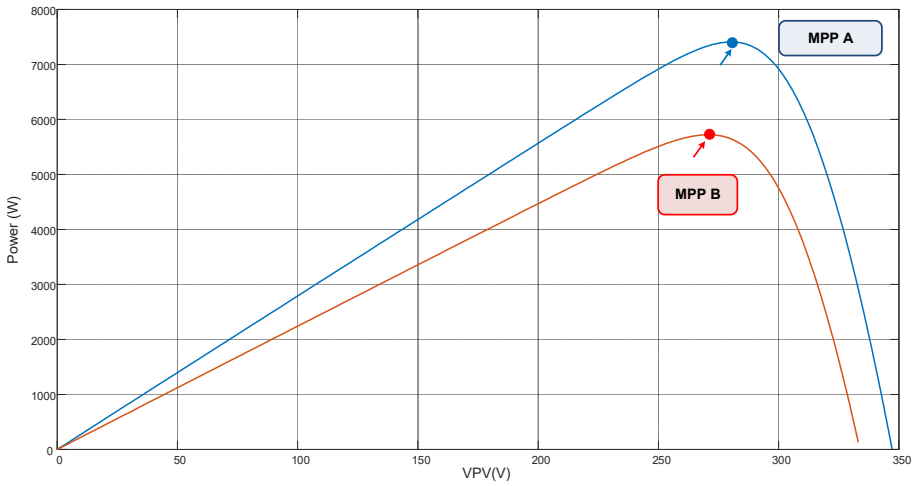


Figure 16. PV power curves for two different points of operation.

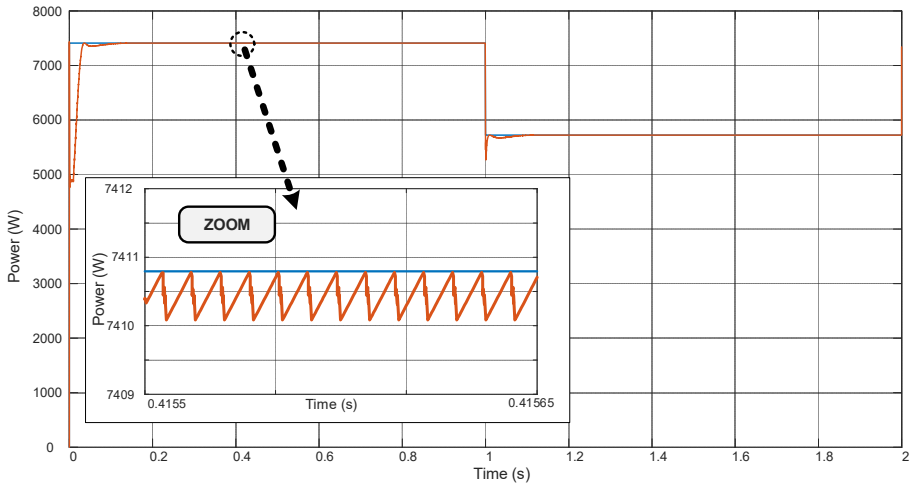


Figure 17. Power extracted and a detail of the power ripple, considering the change in power according to the PV power curves of Figure 16.

3.4. Stationary Battery Operation

This scenario investigates the operation of the stationary battery storage system connected to the DC microgrid. The objective is to demonstrate the ability of the bidirectional

DC–DC converter to manage battery charging and discharging processes, enabling energy storage during periods of high photovoltaic generation and power support during increased system demand. Figures 18, 19 and 20 show the charging and discharging profiles at a C/4 rate. The simulated battery pack has an internal resistance of 0.0196 Ω, a fully charged voltage of 228.14 V, and a nominal voltage of 196 V.

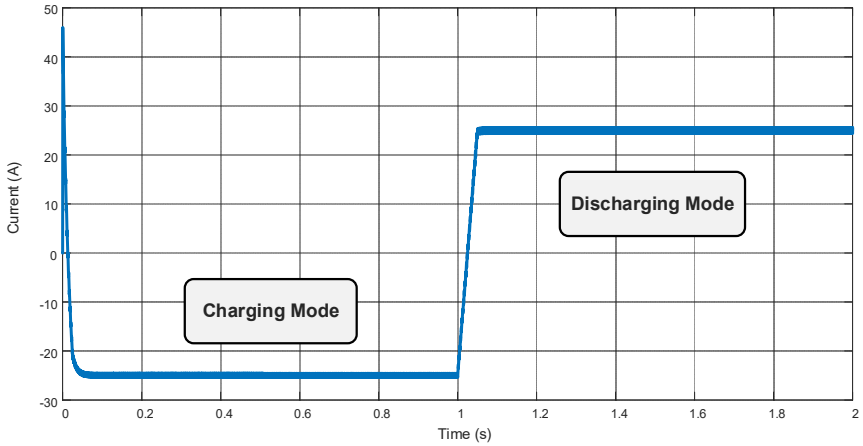


Figure 18. Charging and discharging profiles at a C/4 rate.

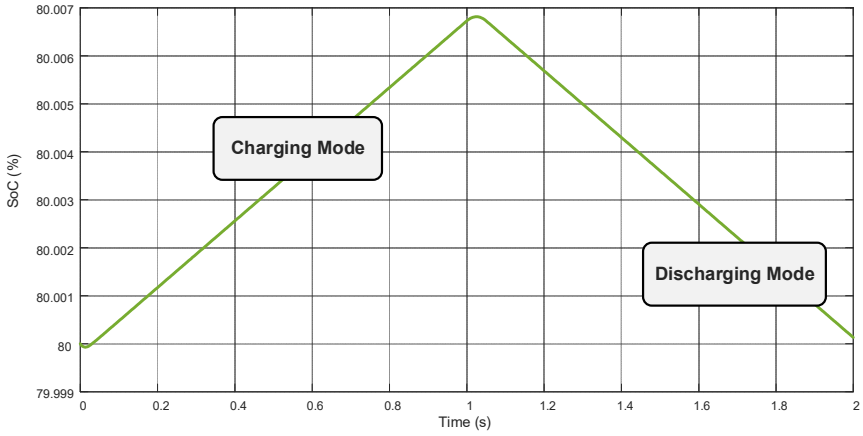


Figure 19. SoC changing with time according to the profiles of Figure 18.

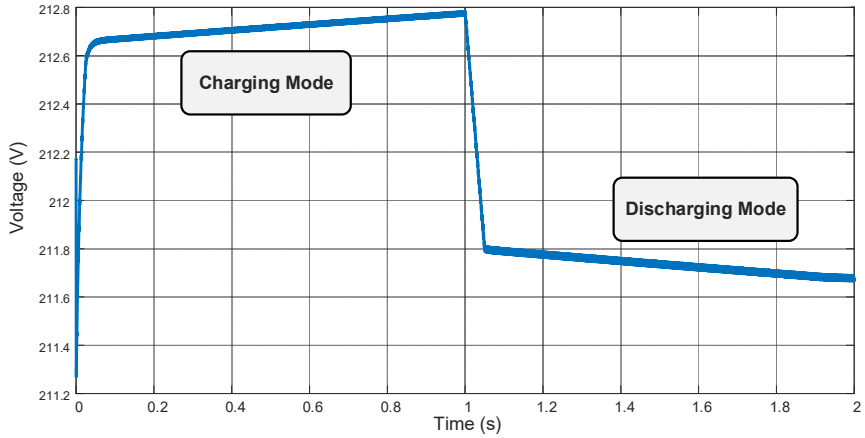


Figure 20. Battery pack voltage changing according to the profiles of Figure 18.

3.5. Grid Support and Reactive Power Control

This scenario evaluates the grid-support functionalities provided by the grid-interface converter. In particular, the capability of the system to regulate reactive power through the q-axis current component is analyzed. The results demonstrate the ability of the charging station to operate with a controllable power factor and contribute to voltage regulation and ancillary services in the distribution grid. Figure 21 presents the reactive power compensation profile of approximately ± 4 kVA.

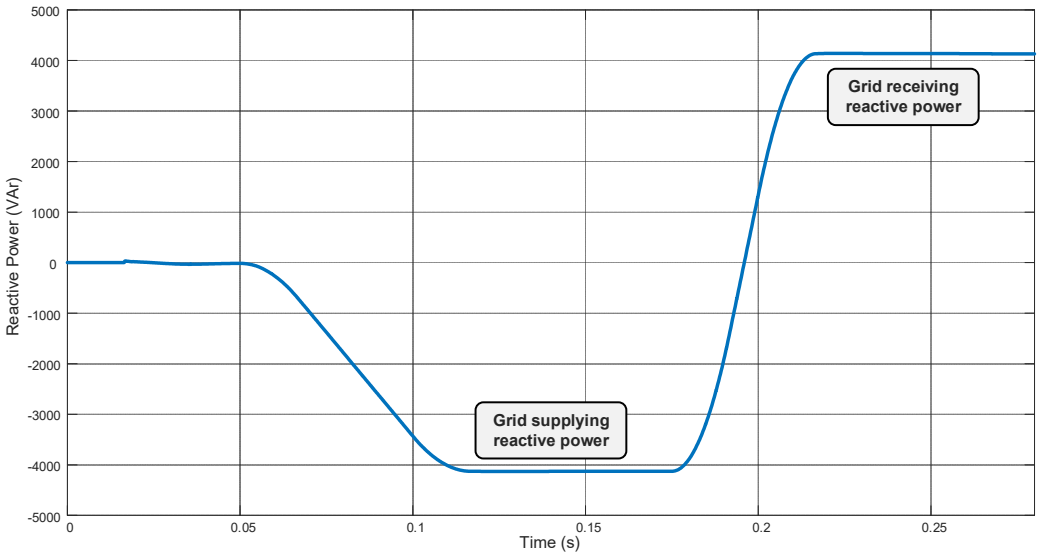


Figure 21. Grid reactive power compensation profile.

3.6. Active Power Filtering Performance

Finally, this scenario analyzes the active filtering capability implemented in the four-leg grid-interface converter. The synchronous reference frame (SRF) method is employed to identify and compensate harmonic components of the grid current as discussed previously.

The grid was modeled as a sinusoidal voltage source without background harmonic distortion, with a series resistance of 0.05 Ω and an inductance of 10 μH. The grid-interface converters and loads were connected at the point of common coupling (PCC). During this scenario, the system simultaneously injected active power into the grid and performed harmonic and reactive current compensation, using the control strategy described in Section 2.2.

The results demonstrate the effectiveness of the proposed control strategy in mitigating current distortions and improving the overall power quality at the point of common coupling. Figure 22 shows the grid currents, while Figure 23 shows the neutral current for a set of unbalanced three-phase linear loads. It is important to observe a neutral current of almost 15 A peak before the APF starts compensating. In addition, Figure 24 shows the grid currents, while Figure 25 shows the neutral current for a set of unbalanced three-phase nonlinear loads with a peak neutral current of 25 A. Tables 6 and 7 summarize the load characteristics. Before the compensation, the grid current of phase A exhibited a THD of 26.90%, phase B a THD of 9.50%, and phase C a THD of 2.55%. After compensation, the grid current THD values were 3.20%, 3.05%, and 2.95% for phases A, B, and C, respectively, indicating substantial harmonic distortion reduction in phases A and B, while phase C exhibited a slight increase in THD. This increase is mainly associated with the reduction in the fundamental current component after compensation. Since phase C supplies a purely resistive load, its initial harmonic distortion was already relatively low. As

THD is defined as the ratio of the harmonic RMS current to the fundamental RMS current, a reduction in the latter can result in a slight increase in THD, even when the harmonic current magnitude remains nearly unchanged. The current THD was calculated individually for each phase using the Simulink Total Harmonic Distortion block, configured with a fundamental frequency of 60 Hz and continuous sample time, considering the total RMS current, its DC component, and the RMS value of the fundamental component. The reported values were obtained after the THD measurements had stabilized, before and after APF activation.

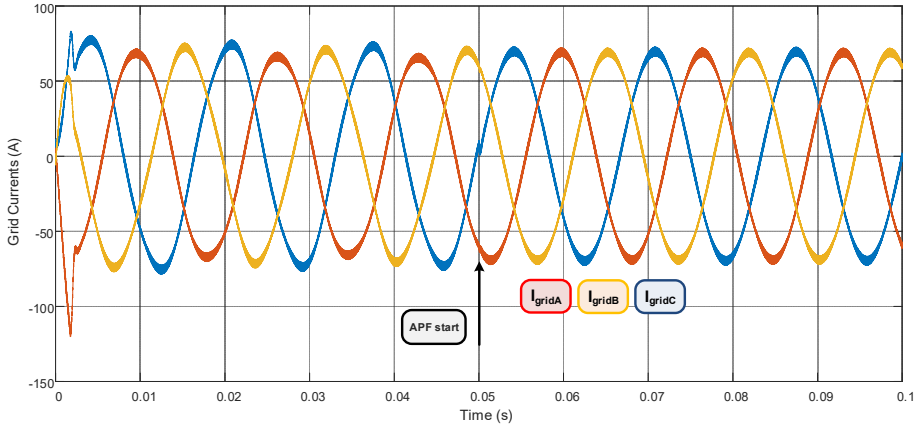


Figure 22. Active filter performance with unbalanced three-phase linear load.

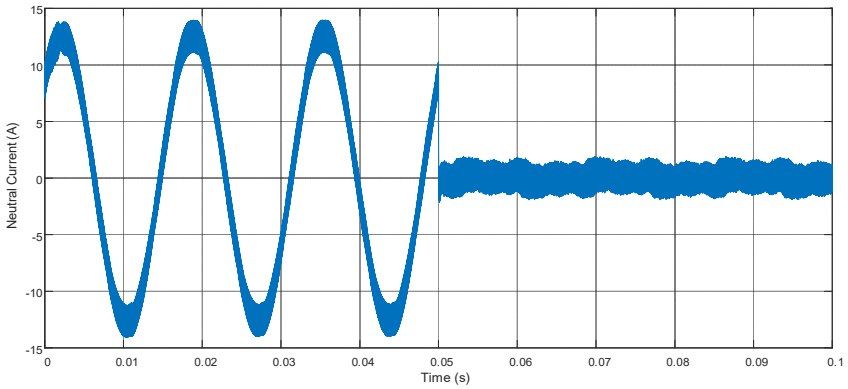


Figure 23. Grid neutral current for the active filter performance with unbalanced three-phase linear load.

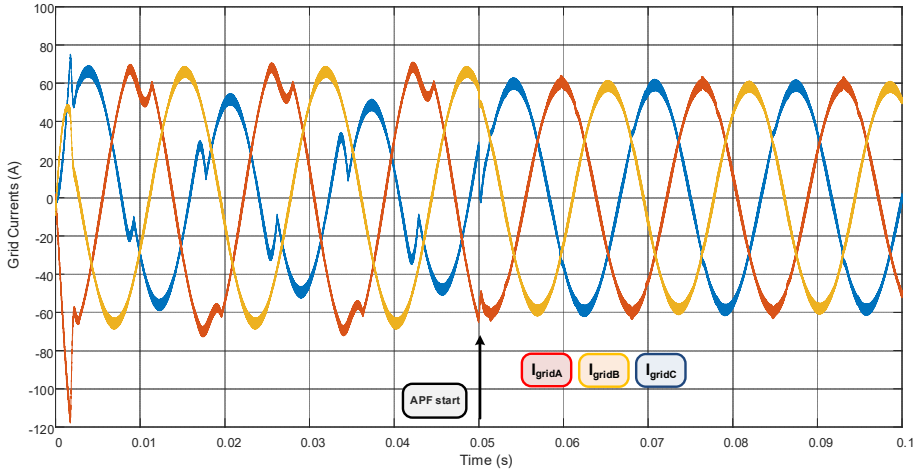


Figure 24. Grid three-phase currents for the active filter with unbalanced three-phase non-linear load.

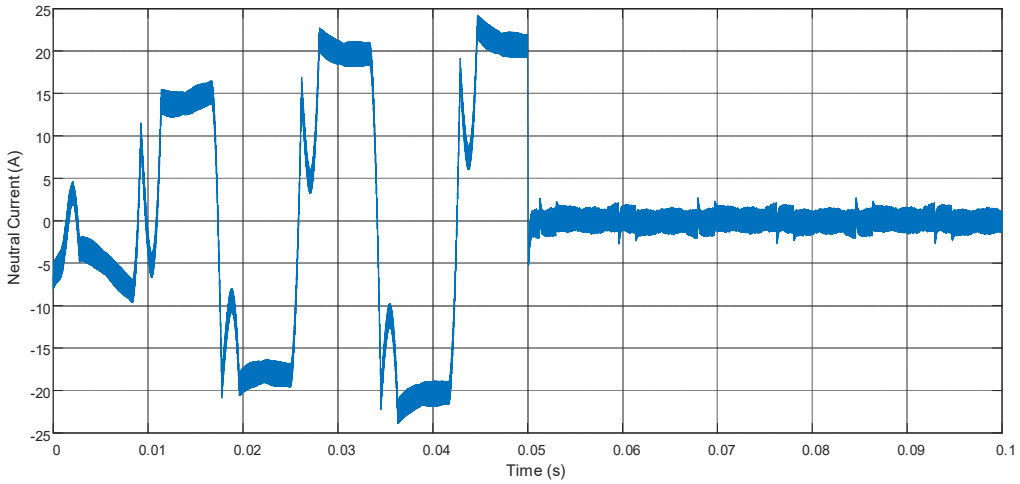


Figure 25. Grid neutral current for the active filter with unbalanced three-phase non-linear load.

Table 6. Linear Load Parameters.

Fase	Load	Values
A to Neutral	RL series	R = 6.47Ω; L = 51.4 mH
B to Neutral	R	R = 32.26Ω
C to Neutral	RC series	R = 14.93; C = 268 μF

Table 7. Non-linear Load Parameters.

Fase	Load	Values
A to Neutral	Single-phase rectifier with RL load	R = 4 Ω; L = 45 mH
B to Neutral	Single-phase rectifier with C filter and R load	R = 60 Ω; C = 1 mF
C to Neutral	R load	R = 20 Ω

3.7. Interleaving Performance

The effectiveness of the interleaving strategy in reducing the grid-current ripple was evaluated under identical operating conditions. Figure 26 compares the phase-B grid-current waveforms with and without interleaving, considering two parallel converters equally sharing the total power. The peak-to-peak current ripple was measured near the peak of the phase-B current (t ≈ 0.082 s). Without interleaving, the ripple was 5.73 A, whereas the interleaved operation reduced it to 3.11 A, corresponding to a 45.7% reduction.

Furthermore, a comparison was performed with a single non-interleaved converter processing the same total power at a switching frequency of 30 kHz. Considering an equivalent filter inductance (L/2), the single converter exhibited a peak-to-peak current ripple of 8.40 A. In comparison, the proposed interleaved configuration reduced the ripple to 3.11 A, representing a 63.0% reduction relative to the single-converter configuration. These results demonstrate the effectiveness of the adopted interleaving strategy in reducing the aggregated grid-current ripple.

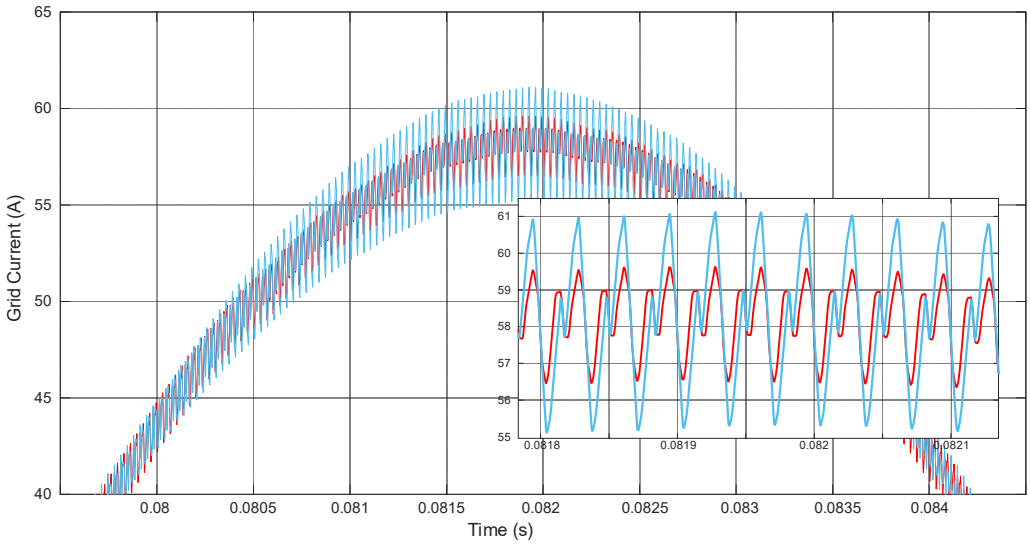


Figure 26. Comparison of the phase-B grid-current ripple with interleaving (red) and without interleaving (blue).

3.8. Multifunctional Performance

This section evaluates the dynamic and simultaneous operation of the proposed system, considering bidirectional active power flow, reactive power compensation, and active power filtering. The objective is to demonstrate the multifunctional capabilities of the proposed architecture while considering the nominal apparent power rating of 11 kVA for each grid-interface converter.

Figure 27 presents the dynamic performance of the grid-interface converters under different operating conditions. Initially, the converters operate by injecting active power into the grid. At 0.25 s, the active power flow is reversed, demonstrating bidirectional power exchange between the DC bus and the utility grid through the grid-interface converters. Subsequently, at 0.5 s, the active power is reduced to zero, followed by the resumption of active power injection and reactive power compensation. At 0.75 s, the active power filtering function is activated, demonstrating the ability of the proposed architecture to perform multiple grid-support functions simultaneously. The corresponding active and reactive power responses, together with the converter currents, illustrate the dynamic behavior during the transitions between operating conditions.

Finally, Figure 28 presents the RMS currents of the four-leg converter during the activation of the active power filtering function. After the activation of the active power filtering function, the RMS current of phase A increased beyond the converter's nominal current of 28.8 A. Therefore, the active current reference was intentionally reduced by adjusting i_d^*, rather than through an automatic current-limiting mechanism, to accommodate the additional compensation currents while maintaining the converter operation within its nominal current limit under steady-state conditions. In this scenario, reactive power compensation and active power filtering were prioritized over active power injection, although this prioritization can be modified according to operational requirements. These results demonstrate that the proposed architecture can operate with bidirectional active power flow and simultaneously provide active power injection and grid-support functions, provided that the converter current limitations are considered.

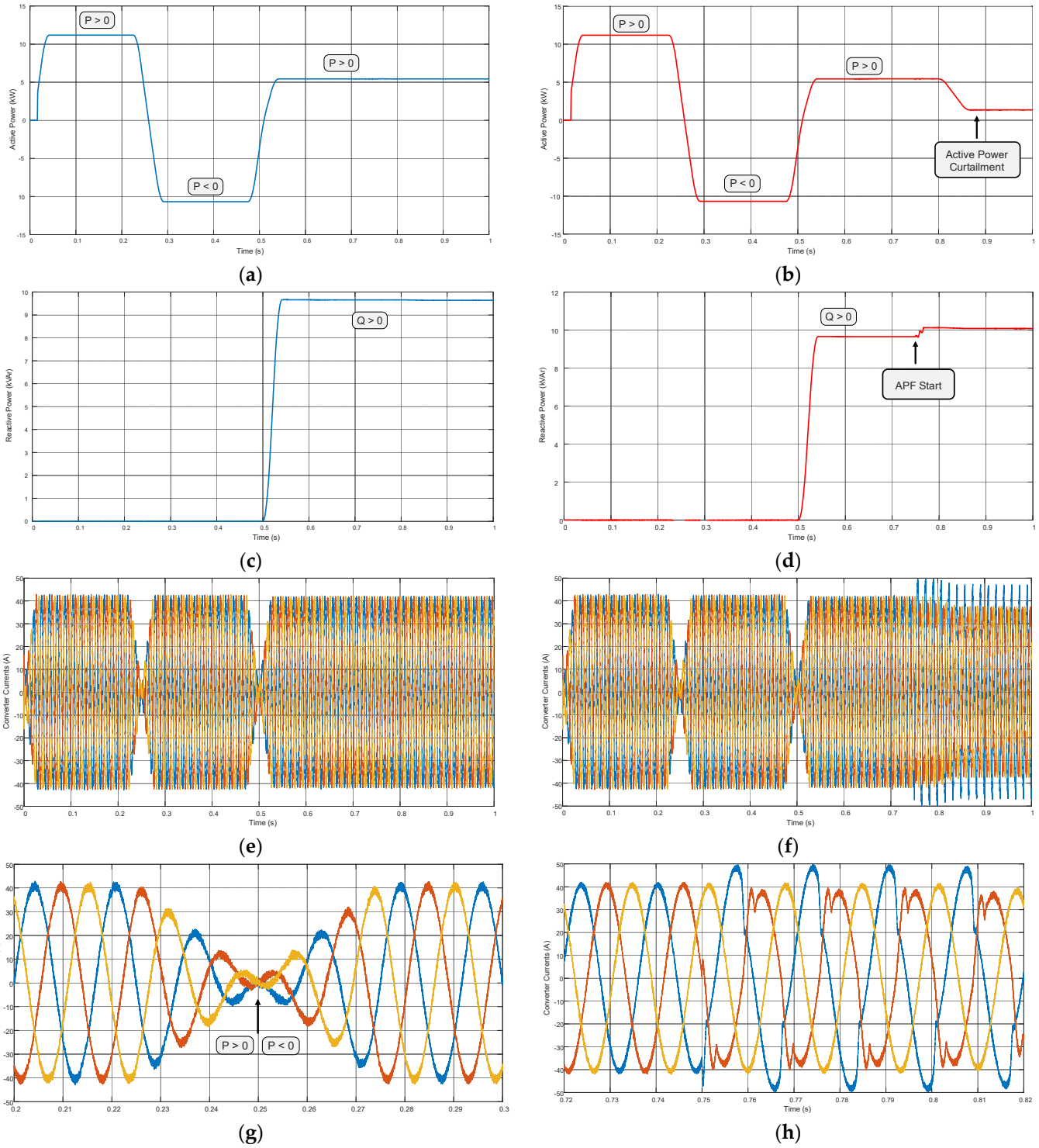


Figure 27. Multifunctional performance of the grid-interface converters: (**a**) active power of the three-leg converter; (**b**) active power of the four-leg converter; (**c**) reactive power of the three-leg converter; (**d**) reactive power of the four-leg converter; (**e**,**f**) converter output currents; and (**g**,**h**) detailed current waveforms during operating transitions.

https://doi.org/10.3390/en19215351

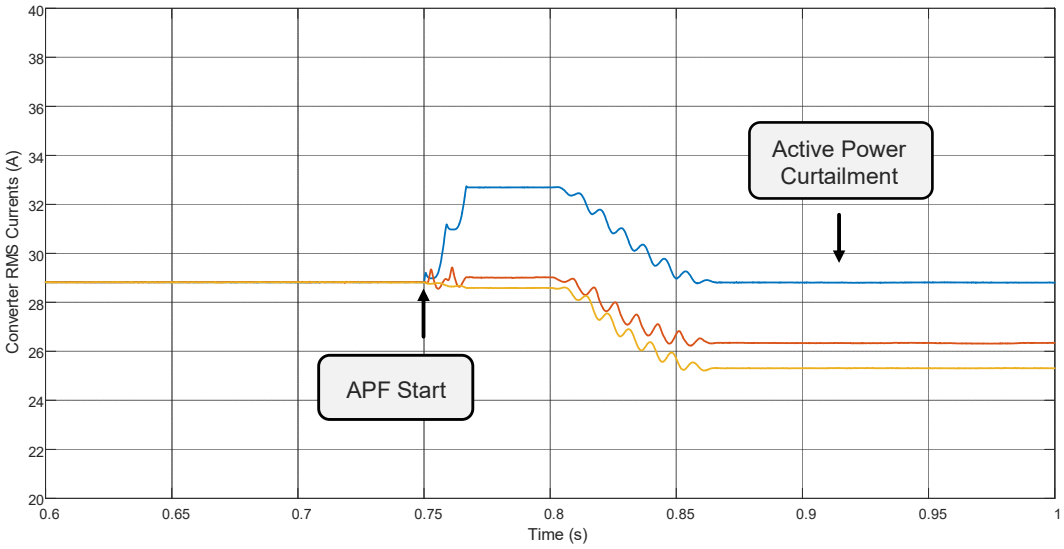


Figure 28. RMS phase currents of the four-leg converter during active power filtering activation and subsequent active power curtailment to comply with the nominal current limit.

These results demonstrate that the proposed architecture can operate with bidirectional active power flow and simultaneously provide active power injection and grid-support functions, provided that the converter current limitations are considered. In particular, the reduction in the active current reference allows the converter to accommodate the additional current components required for compensation without exceeding its nominal current rating under steady-state conditions.

4. Discussions

The simulation results confirm the effectiveness of the proposed EV charging station architecture based on a DC microgrid integrating renewable generation, stationary energy storage, and modular EV charging converters. The DC bus voltage regulation demonstrated stable operation under different operating conditions, including variations in EV charging demand, photovoltaic power generation, and battery charge/discharge transitions. The grid-interface converter successfully maintained the DC bus voltage at its nominal value while enabling bidirectional power flow between the DC microgrid and the utility grid.

The operation of the parallel DAB converters validated the modular EV charging concept, showing balanced power sharing and scalable charging capability. This modular structure allows flexible system expansion while maintaining efficient and controlled power transfer between the DC bus and the vehicle batteries. In addition, the photovoltaic interface converter effectively maximized the energy extracted from the PV system through the implemented MPPT strategy, contributing to the supply of the DC microgrid and reducing the dependence on grid power.

The stationary battery system demonstrated its capability to support energy management strategies, enabling energy storage during periods of high photovoltaic generation and providing additional power during increased system demand. This functionality enhances the flexibility of the charging station and allows better utilization of renewable energy.

Furthermore, the grid-interface converter successfully provided grid-support functionalities, including reactive power control and active filtering capability. The use of the synchronous reference frame (SRF) method enabled the compensation of harmonic current components, resulting in improved current quality at the point of common coupling. These results highlight the potential of EV charging stations not only as energy consumers

but also as active elements that contribute to power quality improvement and ancillary services in modern power systems.

Overall, the proposed architecture demonstrates the feasibility of integrating renewable generation, stationary storage, modular EV charging, and grid-support functionalities within a unified DC microgrid framework. The results indicate that such charging stations can play an important role in future smart grids by enhancing operational flexibility, improving energy efficiency, and supporting grid stability.

5. Conclusions

This paper presented a DC microgrid-based electric vehicle charging station integrating renewable generation, stationary energy storage, and modular EV charging converters. The proposed architecture employs an interleaved bidirectional grid-interface converter, a set of parallel dual active bridge (DAB) converters for EV charging, an interleaved boost converter for photovoltaic integration, and a bidirectional DC–DC converter for stationary battery storage. This structure enables bidirectional power flow, modular scalability, and flexible energy management within the charging station.

The implemented control strategies allow stable DC bus voltage regulation while enabling additional grid-support functionalities, including reactive power control and active power filtering based on the synchronous reference frame method. Simulation results demonstrated the effectiveness of the proposed system under different operating scenarios, including EV charging, photovoltaic power generation, and battery charge/discharge operation. The results also showed improved grid current quality due to harmonic mitigation and reactive power compensation capabilities.

Overall, the simulation results highlight the potential of integrating power electronics, renewable energy, and energy storage to create multifunctional charging infrastructures capable of supporting both electric mobility and the requirements of modern power systems. Future work will focus on experimental validation of the proposed system and the implementation of advanced energy management strategies for the coordinated operation of EV charging, renewable generation, and grid-support services. Such multifunctional charging infrastructures may play an important role in the development of future smart grids and sustainable transportation systems.

Author Contributions: Conceptualization, M.A.G.d.B.; methodology, M.A.G.d.B., R.B.G. and E.C.d.S.; software, G.M.d.S.M. and M.J.d.S.C.; validation, M.A.G.d.B., G.M.d.S.M. and M.J.d.S.C.; formal analysis, M.A.G.d.B., R.B.G. and E.C.d.S.; writing—original draft preparation, M.A.G.d.B.; writing—review and editing, R.B.G. and E.C.d.S.; funding acquisition, M.A.G.d.B. All authors have read and agreed to the published version of the manuscript.

Funding: This study was supported in part by the Foundation for Support to the Development of Education, Science and Technology of the State of Mato Grosso do Sul (FUNDECT) [Process No. 83/044.474/2024, Grant No. 344/2024] and the National Council for Scientific and Technological Development (CNPq) [Grant No. 444696/2024-5]. The article processing charge (APC) was funded by CNPq [Grant No. 444696/2024-5].

Data Availability Statement: The original contributions presented in this study are included in the article material. Further inquiries can be directed to the corresponding author.

Acknowledgments: We would like to thank UFMS and PPGEE-UFMS.

Conflicts of Interest: The authors declare no conflicts of interest.

References

1. Yousuf, A.K.M.; Wang, Z.; Paranjape, R.; Tang, Y. An In-Depth Exploration of Electric Vehicle Charging Station Infrastructure: A Comprehensive Review of Challenges, Mitigation Approaches, and Optimization Strategies. *IEEE Access* **2024**, *12*, 51570–51589. https://doi.org/10.1109/ACCESS.2024.3385731.
2. Gowtham, M.; Suresh, S.; Keer, P.K.; Vaishnavi, K.; Rajasekar, P.; Kayalvizhi, M. A Comprehensive Review on the Evolution of Electric Vehicle Charging Infrastructure. In Proceedings of the 2025 International Conference on Intelligent Computing, Information and Control Systems (ICOIICS), Lalitpur, Nepal, 19–21 November 2025; pp. 587–592. https://doi.org/10.1109/ICOIICS67115.2025.11390241.
3. de Brito, M.A.G; Volpato, A.S.; Batista, E.A.; Godoy, R.B. Power Electronics Converters for an Electric Charging Station: Description and Experimental Evaluation. *Transp. Res. Procedia* **2023**, *70*, 154–161. https://doi.org/10.1016/j.trpro.2023.11.014.
4. Haidar, A.; Macaulay, J.; Fazeli, M. Design and Performance Analysis of a Grid-Integrated Solar PV-Based Bidirectional Off-Board EV Fast-Charging System Using MPPT Algorithm. *Energies* **2026**, *19*, 1656. https://doi.org/10.3390/en19071656.
5. Rajitha, M.; Ram, A.R. DC Microgrid Technology: Study on DC Microgrid Bus Configurations and Architectures for Rural Electrification and a Proposed DC Microgrid Architecture. In Proceedings of the 2024 International Conference on Social and Sustainable Innovations in Technology and Engineering (SASI-ITE), Tadepalligudem, India, 23–25 February 2024; pp. 168–173. https://doi.org/10.1109/SASI-ITE58663.2024.00037.
6. Mouelhi, A.; Kraiem, Y.; Faouzi Mimouni, M. Optimization of PV benefits for electric vehicles charging station using a deterministic method and fuzzy inference system method. *J. Eng. Res.* **2025**, *13*, 3308–3333. https://doi.org/10.1016/j.jer.2024.10.018.
7. Buja, G.; Bertoluzzo, M.; Fontana, C. Reactive Power Compensation Capabilities of V2G-Enabled Electric Vehicles. *IEEE Trans. Power Electron.* **2017**, *32*, 9447–9459. https://doi.org/10.1109/TPEL.2017.2658686.
8. Wouters, H.; Martinez, W. Bidirectional Onboard Chargers for Electric Vehicles: State-of-the-Art and Future Trends. *IEEE Trans. Power Electron.* **2024**, *39*, 693–716. https://doi.org/10.1109/TPEL.2023.3319996.
9. Fesli, U.; Ozdemir, M.B. Electric Vehicles: A Comprehensive Review of Technologies, Integration, Adoption, and Optimization. *IEEE Access* **2024**, *12*, 140908–140931. https://doi.org/10.1109/ACCESS.2024.3469054.
10. Conti, S.; Aiello, G.; Coco, S.; Laudani, A.; Rizzo, S.A.; Salerno, N.; Tina, G.M.; Ventura, C. Optimization and Machine Learning for Electric Vehicles Management in Distribution Networks: A Review. *Energies* **2026**, *19*, 986. https://doi.org/10.3390/en19040986.
11. Jain, V.; Singh, B.; Seema. A Grid Connected PV Array and Battery Energy Storage Interfaced EV Charging Station. *IEEE Trans. Transp. Electrif.* **2023**, *9*, 3723–3730. https://doi.org/10.1109/TTE.2023.3234994.
12. Ru, J.; Gillott, M.; Shipman, R. Vehicle-to-Grid (V2G) Research: A Decade of Progress, Achievements, and Future Directions. *Energies* **2025**, *18*, 6148. https://doi.org/10.3390/en18236148.
13. Singh, S.; Bansal, H.O. Hardware-in-loop implementation of an adaptive MPPT controlled PV-assisted EV charging system with vehicle-to-grid integration. *Sci. Rep.* **2025**, *15*, 28565. https://doi.org/10.1038/s41598-025-12508-3.
14. Sun, Q.; Yu, X.; Li, H.; Peng, F.; Sun, G. Fault detection for power electronic converters based on continuous wavelet transform and convolution neural network. *J. Intell. Fuzzy Syst. Appl. Eng. Technol.* **2022**, *42*, 3537–3549. https://doi.org/10.3233/JIFS-211632.
15. Fan, C.; Wang, Y.; Peng, Q.; Liu, K. Towards Plating-Free Fast Charging for Lithium-Ion Batteries: A Review of Optimization Aspects. *IEEE Trans. Transp. Electrif.* **2026**, 1-1. https://doi.org/10.1109/TTE.2026.3736242.
16. Liserre, M.; Blaabjerg, F.; Hansen, S. Design and control of an LCL-filter-based three-phase active rectifier. *IEEE Trans. Ind. Appl.* **2005**, *41*, 1281–1291. https://doi.org/10.1109/TIA.2005.853373.
17. Wu, W.; Liu, Y.; He, Y.; Chung, H.S.-H.; Liserre, M.; Blaabjerg, F. Damping Methods for Resonances Caused by LCL-Filter-Based Current-Controlled Grid-Tied Power Inverters: An Overview. *IEEE Trans. Ind. Electron.* **2017**, *64*, 7402–7413. https://doi.org/10.1109/TIE.2017.2714143.
18. Nalamati, C.S.; Gupta, R. Analytical investigation of interleaved input/output parallel DAB converter for grid scale battery storage. *J. Energy Storage* **2024**, *99*, 113400. https://doi.org/10.1016/j.est.2024.113400.
19. Shao, S.; Chen, L.; Shan, Z.; Gao, F.; Chen, H.; Sha, D.; Dragičević, T. Modeling and Advanced Control of Dual-Active-Bridge DC–DC Converters: A Review. *IEEE Trans. Power Electron.* **2022**, *37*, 1524–1547. https://doi.org/10.1109/TPEL.2021.3108157.
20. *ABNT NBR IEC 61851-1*; Electric Vehicle Conductive Charging System Part 1: General Requirements. Second Edition. 2021.
21. Blaabjerg, F.; Teodorescu, R.; Liserre, M.; Timbus, A.V. Overview of Control and Grid Synchronization for Distributed Power Generation Systems. *IEEE Trans. Ind. Electron.* **2006**, *53*, 1398–1409. https://doi.org/10.1109/TIE.2006.881997.
22. Golestan, S.; Monfared, M.; Freijedo, F.D. Design-Oriented Study of Advanced Synchronous Reference Frame Phase-Locked Loops. *IEEE Trans. Power Electron.* **2013**, *28*, 765–778. https://doi.org/10.1109/TPEL.2012.2204276.

23. da Silva, S.A.O.; Neto, A.F.; Cervantes, S.G.S.; Goedtel, A.; Nascimento, C.F. Synchronous reference frame based controllers applied to shunt active power filters in three-phase four-wire systems. In Proceedings of the 2010 IEEE International Conference on Industrial Technology, Via del Mar, Chile, 14–17 March 2010; pp. 832–837. https://doi.org/10.1109/ICIT.2010.5472605.
24. Wang, X.; Liu, J.; Hu, J.; Meng, Y.; Yuan, C. Frequency characteristics of the d-q synchronous-frame current reference generation methods for active power filter. In Proceedings of the 2007 7th International Conference on Power Electronics, Daegu, Republic of Korea, 22–26 October 2007; pp. 945–950. https://doi.org/10.1109/ICPE.2007.4692523.
25. O'Rourke, C.J.; Qasim, M.M.; Overlin, M.R.; Kirtley, J.L. A Geometric Interpretation of Reference Frames and Transformations: Dq0, Clarke, and Park. *IEEE Trans. Energy Convers.* **2019**, *34*, 2070–2083. https://doi.org/10.1109/TEC.2019.2941175.
26. Wang, P.; Qin, Z.; Yuan, J.; Blaabjerg, F. Dual active bridge converter and its control. In *Control of Power Electronic Converters and Systems*; Elsevier: Amsterdam, The Netherlands, 2024; Volume 4, pp. 71–100. https://doi.org/10.1016/B978-0-323-85622-5.00012-2.
27. Esram, T.; Chapman, P.L. Comparison of Photovoltaic Array Maximum Power Point Tracking Techniques. *IEEE Trans. Energy Convers.* **2007**, *22*, 439–449. https://doi.org/10.1109/TEC.2006.874230.
28. Elgendy, M.A.; Zahawi, B.; Atkinson, D.J. Assessment of the Incremental Conductance Maximum Power Point Tracking Algorithm. *IEEE Trans. Sustain. Energy* **2013**, *4*, 108–117. https://doi.org/10.1109/TSTE.2012.2202698.
29. Sera, D.; Mathe, L.; Kerekes, T.; Spataru, S.V.; Teodorescu, R. On the Perturb-and-Observe and Incremental Conductance MPPT Methods for PV Systems. *IEEE J. Photovolt.* **2013**, *3*, 1070–1078. https://doi.org/10.1109/JPHOTOV.2013.2261118.
30. de Brito, M.A.G.; Alves, M.G.; Canesin, C.A. Hybrid MPPT Solution for Double-Stage Photovoltaic Inverter. *J. CONTROL Autom. Electr. Syst.* **2019**, *30*, 253–265. https://link.springer.com/article/10.1007/s40313-019-00447-0.
31. Martines, G.M.S.; de Brito, M.A.G.; Batista, E.A.; Godoy, R.B.; Mateus, T.H.A. Sensorless MPPT Algorithms for PV Systems in Partially Shaded Scenarios. *Eletrônica de Potência* **2024**, *9*, e202452. https://doi.org/10.18618/REP.e202452.

Disclaimer/Publisher's Note: The statements, opinions and data contained in all publications are solely those of the individual author(s) and contributor(s) and not of MDPI and/or the editor(s). MDPI and/or the editor(s) disclaim responsibility for any injury to people or property resulting from any ideas, methods, instructions or products referred to in the content.